Magnetic neutron-scattering study of $MnCl_2$-graphite intercalation compound

David G. Wiesler*
Department of Physics, The George Washington University, Washington, DC 20052

Masatsugu Suzuki and Itsuko S. Suzuki
Department of Physics, State University of New York at Binghamton, Binghamton, New York 13902-6016

Nicholas Rosov
Reactor Radiation Division, National Institute of Standards and Technology, Gaithersburg, Maryland 20899
(Received 11 September 1996)

The in-plane spin order of $MnCl_2$ graphite intercalation compound has been studied between 63 mK and 30 K by elastic neutron scattering. This compound approximates a classical XY antiferromagnet on a triangular lattice. Below 7.5 K magnetic critical scattering peaks are observed at wave vectors incommensurate with the $MnCl_2$ and graphene sublattices. As the temperature is raised, the cell contracts towards a commensurate $2\sqrt{3}\times 2\sqrt{3}$ magnetic unit cell. The ground-state in-plane spin configuration is explained by an exchange Hamiltonian that includes no fewer than three shells of nearest neighbors in the plane. The magnetic peaks have a Lorentzian shape and are broader than resolution down to 63 mK, well below the peak in the magnetic susceptibility at 1.1 K. No evidence of three-dimensional magnetic correlations was found at any temperature. [S0163-1829(97)01510-5]

I. INTRODUCTION

$MnCl_2$ is a $CdCl_2$-type layered material in which Mn^{2+} ions lie in close-packed triangular layers, separated by two layers of Cl^- ions. The hexagonal unit cell contains three molecular units with lattice constants $a=3.6934$ Å (representing the near-neighbor distance between magnetic ions) and $c=17.475$ Å (corresponding to three times the distance between consecutive Mn^{2+} layers). Despite the fact that $MnCl_2$ has been studied by a variety of methods[1–3] for over fifty years, its magnetic structure is not completely understood.

Two interesting features, in particular, have escaped explanation. First, $MnCl_2$ undergoes two phase transitions, with Néel temperatures, $T_{N1}=1.96$ K and $T_{N2}=1.81$ K, that are quite low when one considers the large magnetic moments ($S=\frac{5}{2}$) of the Mn^{2+} ions. Other isomorphous transition metal chlorides order at much higher temperatures [e.g., 24 K for $FeCl_2$,[4] 25 K for $CoCl_2$,[5] and 52 K for $NiCl_2$ (Ref. 6)], despite smaller moments. Second, the two antiferromagnetic phases (between T_{N1} and T_{N2} and below T_{N2}) are characterized by very large unit cells (60 and 90 atoms, respectively), as reported in preliminary neutron scattering studies by Wilkinson *et al.*[2,3] The existence of such large cells requires a complicated spin Hamiltonian.

One way to simplify interpretation of the magnetic structure is to reduce the interplanar interaction through intercalation of $MnCl_2$ into graphite. In a stage-n $MnCl_2$-graphite intercalation compound (GIC), magnetic $MnCl_2$ layers are separated by n graphite layers in stacks along the c axis. The interplanar exchange interaction between adjacent $MnCl_2$ layers is greatly reduced by these intervening graphite layers, while the intraplanar exchange interaction may be virtually unchanged. In $MnCl_2$-GIC, the intercalate layer forms a triangular lattice, nearly identical to that in pristine $MnCl_2$. Therefore, understanding the magnetic structure of the GIC may shed light on the magnetic structure of $MnCl_2$ itself.

With the c-axis coupling dramatically reduced, $MnCl_2$-GIC may also be a suitable prototype for studying the classical two-dimensional (2D) XY antiferromagnet on a triangular lattice (AFT).[7] This model system has received attention from theorists because the spins in it are fully frustrated. The ground state of the 2D AFT consists of spins on three sublattices forming 120° angles with respect to each other (the $\sqrt{3}\times\sqrt{3}$ spin structure).[8] Because there are two senses to the spin helicity, the ground state has a twofold discrete degeneracy as well as an XY-like continuous degeneracy. Consequently, it is predicted to undergo two phase transitions, one associated with Ising-type symmetry breaking and the other with a Kosterlitz-Thouless mechanism.[9]

The magnetic properties of stage-2 $MnCl_2$-GIC have been studied by dc and ac magnetic susceptibility,[10–13] heat capacity,[13] electron spin resonance (ESR),[14] and magnetic neutron scattering.[15–17] A peak in the susceptibility at $T_m=1.1$ K suggests a magnetic phase transition. High-temperature susceptibility data give a negative Curie-Weiss temperature $\Theta=-5.94$ K, indicating a net antiferromagnetic interaction and an effective magnetic moment of $5.83\mu_B$, close to the spin-only value 5.92 of $2[S(S+1)]^{1/2}$ for $S=\frac{5}{2}$. ESR measurements show that the g factor has a weak anisotropy at high temperature ($g_c=1.912\pm0.005$ along the c axis and $g_a=1.977\pm0.005$ in the intercalate plane) that becomes more pronounced as the temperature is lowered below 50 K. At 300 K the ESR linewidth is given by $(3\cos^2\phi-1)^2$, where ϕ is the angle between the external magnetic field and the c axis; this form indicates the 2D character of this compound.[14] The heat capacity of stage-2 $MnCl_2$-GIC shows no appreciable anomaly at T_m, but exhibits a broad plateau between 5 and 10 K presumably associated with the growth of 2D spin short-range order.[13]

 © 1997 The American Physical Society

In light of these measurements, the spin Hamiltonian of Mn^{2+} ions in stage-2 $MnCl_2$-GIC has been written as[10]

$$H=-2J\sum_{\langle i,j\rangle}\mathbf{S}_i\cdot\mathbf{S}_j+D\sum_{\langle i,j\rangle}(S_i^z)^2-2J'\sum_{\langle i,m\rangle}\mathbf{S}_i\cdot\mathbf{S}_m, \quad (1)$$

with spin $S=\frac{5}{2}$, where the z axis coincides with the c axis, D is the single ion anisotropy ($D=0.97$ K), J is the nearest-neighbor intraplanar interaction (estimated as $J=-0.20$ K) and J' is the interplanar exchange interaction. The summations are over nearest-neighbor intraplanar pairs, i and j, and nearest-neighbor interplanar pairs, i and m. Dipole-dipole interactions have not been included.

In a previous report[15] we presented preliminary results of magnetic neutron scattering measurements on $MnCl_2$-GIC between 0.6 and 20 K. We concluded there that the in-plane spin structure below T_m was commensurate with the $MnCl_2$ lattice with a $2\sqrt{3}\times 2\sqrt{3}$ periodicity. Such a structure, however, is incompatible with the Hamiltonian given in Eq. (1), as we will show below. In order to understand the system better, we have undertaken further measurements on the same sample, extending the temperature range down to 63 mK. We show here that the magnetic reflections appear at in-plane wave vectors near, but shorter than, those for the $2\sqrt{3}\times 2\sqrt{3}$ spin structure. The wave vectors lengthen towards a commensurate value as the temperature increases, suggesting that the incommensurate low-temperature structure ''coils up'' with increasing temperature toward a locally ordered arrangement commensurate with the $MnCl_2$ lattice. We discuss possible origins of this structure and conclude that the spin Hamiltonian must be modified to include at least up to third nearest neighbors in the plane.[16]

II. EXPERIMENTAL PROCEDURE

$MnCl_2$-GIC samples were synthesized by heating single-crystal kish graphite and anhydrous $MnCl_2$ in a chlorine gas atmosphere at a pressure of 740 Torr. The reaction was continued at 520 °C for 20 days. Stage fidelity of the samples was checked both by weight uptake and by $(00l)$ x-ray diffraction. Afterwards, about 30 of these samples were stacked together on a thin Al foil to increase the sample size. The resulting crystal texture had a c-axis mosaic spread of 10° and random orientation in the a-b plane.

Elastic neutron scattering experiments were performed on the triple axis spectrometers BT-2 and BT-9 at the National Institute of Standards and Technology. A ^{3}He cryostat was used at BT-2 to collect data between 0.43 and 30 K, and a dilution refrigerator was used at BT-9 to extend the range down to 63 mK. Highly oriented pyrolytic graphite monochromators and analyzers, set for zero energy transfer, were used. Incident neutron wavelengths were $\lambda=2.433$ Å at BT-2 and $\lambda=2.352$ Å at BT-9. Graphite filters were used to eliminate the $\lambda/2$ contamination after the monochromator. The collimation was $60'-40'-40'-80'$ at BT-2 and $40'-48'-48'-400'$ at BT-9, giving longitudinal instrumental resolutions (full width at half maximum) of approximately 0.033 Å^{-1} (BT-2) and 0.039 Å^{-1} (BT-9) at the first magnetic reflection. The energy resolution at the elastic position was 1.1 meV on BT-2 and 1.6 meV on BT-9, large enough in both cases to integrate over all critical scattering.

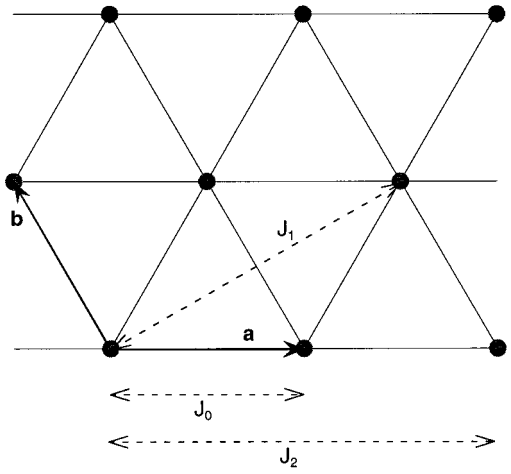

FIG. 1. The Mn^{2+} ions in the intercalate plane of $MnCl_2$ GIC. The vectors **a** and **b** are the primitive translation vectors, and J_0, J_1, and J_2 are the intraplanar exchange interactions.

III. RESULTS

Figure 1 shows the triangular Mn^{2+} lattice in $MnCl_2$-GIC. Primitive lattice vectors **a** and **b** have length $|\mathbf{a}|=|\mathbf{b}|=3.692\pm0.005$ Å, the same as for pristine $MnCl_2$ (3.693 Å).[18] The reciprocal lattice of $MnCl_2$ -GIC is shown in Fig. 2, where $\mathbf{a}_G^*$ and $\mathbf{b}_G^*$ are reciprocal lattice vectors of the graphene lattice and $\mathbf{a}^*$ and $\mathbf{b}^*$ are reciprocal lattice vectors of the Mn^{2+} lattice: $|\mathbf{a}_G^*|=|\mathbf{b}_G^*|=2.952$ Å^{-1}, $|\mathbf{a}^*|=|\mathbf{b}^*|=4\pi/\sqrt{3}a=1.965$ Å^{-1}, and the angle between $\mathbf{a}_G^*$ and $\mathbf{a}^*$ is 30°.[19] The $MnCl_2$ and graphene sublattices are incommensurate and rotated 30° from each other.

Figure 3 shows the $(00l)$ neutron scattering intensity at 30 K, well above T_c. The most intense peaks can be indexed to stage-2 reflections $(00l)_2$, with a c axis repeat distance of $d=12.71\pm0.08$ Å, and to stage-1 reflections $(00l)_1$, with

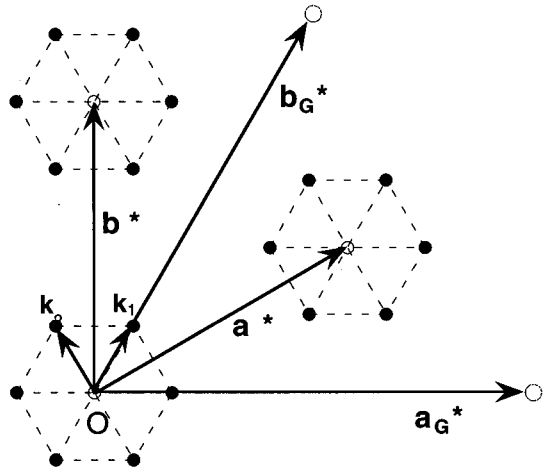

FIG. 2. Reciprocal lattice plane for $MnCl_2$-GIC. Large open circles are nuclear reciprocal lattice vectors from the graphene layers, small open circles are from the $MnCl_2$ layer, and closed circles are magnetic reflections. $|\mathbf{a}_G^*|=|\mathbf{b}_G^*|=2.952$ Å^{-1}, $|\mathbf{a}^*|=|\mathbf{b}^*|=1.965$ Å^{-1}, and $|\mathbf{k}_i|=0.522$ Å^{-1} at the lowest temperatures.

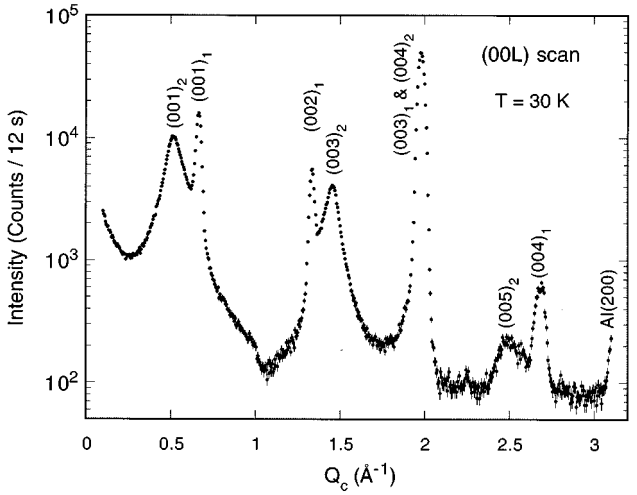

FIG. 3. Neutron scattering intensity at 30 K in the $[00l]$ direction. Peaks are indexed with subscripts that give their stage number. The scattering at 0.43 K is essentially identical.

$d=9.42\pm0.04$ Å. Peaks are broadened by Hendricks-Teller disorder.[20] Whereas $(00l)$ scans by x-ray diffraction show mostly stage-1 peaks, we find from the neutron intensity ratio that our sample consists of 60% nominal stage-2 and 40% nominal stage-1. The difference indicates that the outside of the kish samples is predominantly stage-1, while the inside is mostly stage-2. Subtraction of the neutron data from similar scans taken at 0.43 K shows no magnetic intensity along $(00l)$.

Figure 4 shows a scan in the in-plane wave vector $\mathbf{Q}_\parallel$ at 30 K in the powder-averaged $[hk0]$ direction. The two prominent peaks can be indexed to the Mn(100), and G(100) reflections, where the characters preceding the Miller indices indicate to which sublattice the peaks are indexed. Also present are Al(111) and Al(200) reflections from the aluminum sample can and $(00l)_1$ and $(00l)_2$ reflections, which

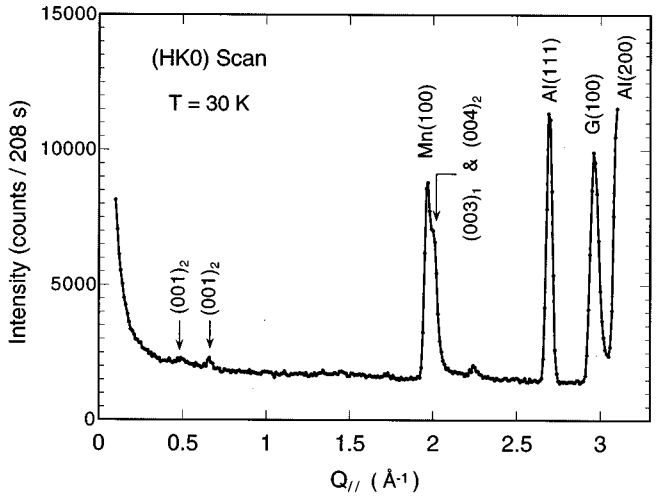

FIG. 4. In-plane neutron scattering intensity at 30 K. Peaks are indexed to the intercalate layer, the graphene layer, or the Al sample can. Because of the large c-axis mosaic spread, some $(00l)$ reflections are seen.

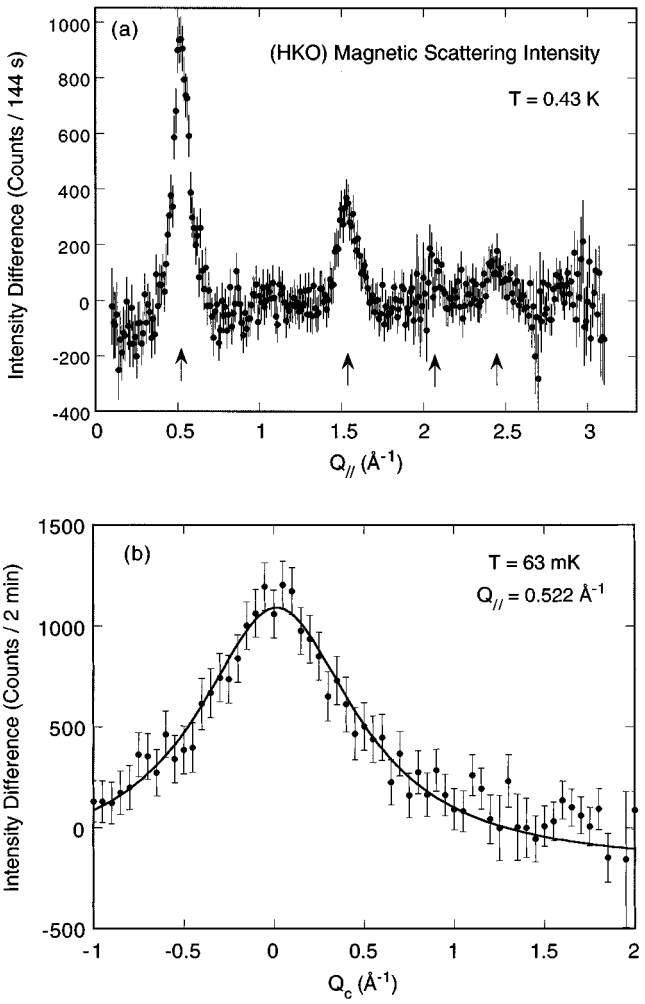

FIG. 5. (a) Magnetic scattering along $(hk0)$ at 0.43 K. Arrows mark the peak positions predicted from Fig. 2. (b) Magnetic scattering at 63 mK versus out-of-plane scattering vector Q_c with $|\mathbf{Q}_\parallel|$ fixed at 0.522 Å^{-1}, its value at the first magnetic peak. The featureless decrease in intensity away from the origin is due to mosaicity and magnetic form factor.

appear as weak powder rings along $[hk0]$ because of the large c-axis mosaicity.

The in-plane magnetic scattering at 0.43 K is shown in Fig. 5(a). These data were obtained by subtracting the intensity at 14.85 K from the corresponding intensity at 0.43 K. Magnetic peaks are observed at $|\mathbf{Q}_\parallel|=0.522$, 1.536, 2.05, and 2.44 Å^{-1}. These wave vectors are consistent with the picture shown in Fig. 2. According to this, the magnetic Bragg reflections should appear at the in-plane wave vectors $\mathbf{Q}_\parallel=h\mathbf{a}^*+k\mathbf{b}^*\pm\mathbf{k}_1$, $\pm\mathbf{k}_2$, or $\pm(\mathbf{k}_1-\mathbf{k}_2)$, h and k are integers and where $\mathbf{k}_i$ $(i=1,2)$ are the reciprocal lattice vectors of magnetic superlattice. Assigning $|\mathbf{k}_1|=0.522$ Å^{-1} and $|\mathbf{a}^*-\mathbf{k}_1|=1.536$ Å^{-1} from our data, the angle θ between $\mathbf{k}_1$ and $\mathbf{a}^*$ is:

$$\cos\theta=\frac{|\mathbf{a}^*|^2+|\mathbf{k}_1|^2-|\mathbf{a}^*-\mathbf{k}_1|^2}{2|\mathbf{k}_1||\mathbf{a}^*|}, \tag{2}$$

or $\theta=30\pm2°$, as drawn in Fig. 2. The next lowest-angle magnetic Bragg reflections are predicted to occur at $|\mathbf{a}^*+\mathbf{k}_2|=2.033$ Å^{-1} and $|\mathbf{a}^*+\mathbf{k}_1|=2.431$ Å^{-1}, in good

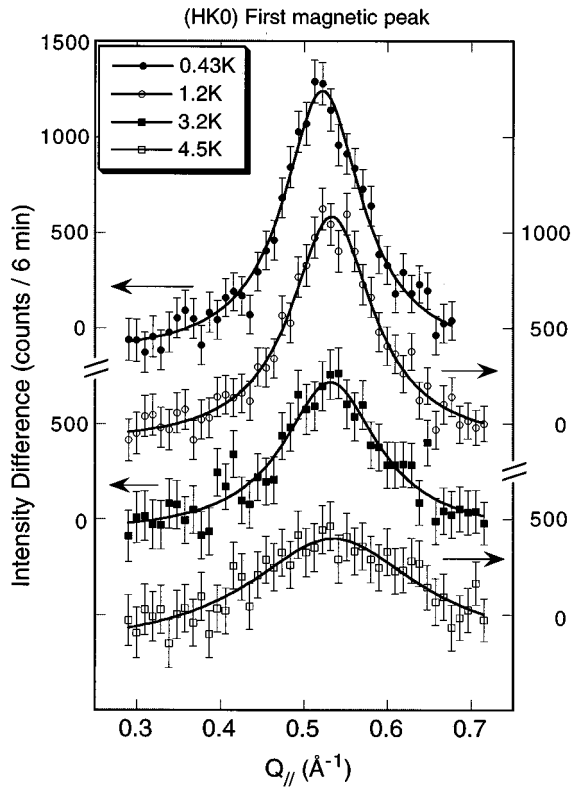

FIG. 6. Magnetic neutron scattering intensity along $(hk0)$ at various temperatures. Scans are offset from each other by 500 counts for clarity. Least-squares fits to Lorentzian peaks are denoted by solid lines.

agreement with the observed values. The principal magnetic wave vector $\mathbf{k}_1$ is therefore indexed as Mn(0.153, 0.153, 0). Its magnitude is slightly less than that for a commensurate $2\sqrt{3}\times 2\sqrt{3}$ cell, Mn(1/6, 1/6, 0), which we reported earlier[15] on the basis of a less complete data set. The origin of the incommensurate spin structure will be discussed in Sec. V.

The mixture of stages shown in Fig. 3 is potentially a problem in analyzing the spin structure. However, if interplanar interactions are negligibly small in the stage-1 regions, they will certainly be so in the stage-2 regions as well, and the in-plane magnetic structure we observe should be valid for both compounds. Figure 5(b) shows the magnetic scattering at 63 mK for a scan of out-of-plane wave vector $\mathbf{Q}_c$ with the in-plane wave vector $\mathbf{Q}_\parallel$ fixed at $\mathbf{k}_1$. The only feature is a decrease in intensity away from the origin, due to the falloff of the magnetic form factor and the effects of the large c-axis mosaic spread, which causes 2D rods to be broadened away from $Q_c=0$. More importantly, there is no modulation of the intensity in Fig. 5(b). This result indicates that there is essentially no magnetic ordering between adjacent layers.

The temperature dependence of the scattering was investigated by a series of $(hk0)$ scans at temperatures between 63 mK and 7.5 K. Representative scans are shown in Fig. 6, in which the magnetic intensity was determined by subtracting analogous data taken at 14.85 K. Throughout the entire temperature range, the intensities fit well to a Lorentzian peak described by

$$I=\frac{I_0\kappa}{\pi\{(|\mathbf{Q}_\parallel|-\tau)^2+\kappa^2\}}-\text{ const}, \tag{3}$$

where κ is the inverse in-plane spin correlation length, τ is the peak position, and I_0 is the integrated intensity. The constant term represents paramagnetic scattering at 14.85 K and is assumed to be independent of $|\mathbf{Q}_\parallel|$ over the range of the scan. (This negative background shows up in all the magnetic scans and is due to the transfer of the q-independent paramagnetic scattering into the magnetic peaks with decreasing temperature. Instrumental broadening is negligible for all peaks.)

The solid lines in Fig. 6 are the best fits of the data to Eq. (3), taking τ, κ, I_0, and the constant as free parameters. Figure 7(a) shows the temperature dependence of the peak position τ. The value of τ is nearly constant at 0.522 $Å^{-1}$ below 0.43 K and increases rapidly with temperature in the vicinity of 1.1 K. Above T_m, τ plateaus briefly at 0.532 $Å^{-1}$, rising again above 4.5 K toward the commensurate Mn(1/6, 1/6, 0) position at $|\mathbf{a}^*|/2\sqrt{3}=0.567$ $Å^{-1}$.

Figure 7(b) shows the temperature dependence of the peak intensity $I_0/\pi\kappa$ at the first magnetic reflection. The peak intensity rises as the temperature is lowered; however, it does not rise precipitously below T_m, as one would expect for the growth of long-range spin order. Only short-range order is seen as well for the inverse spin correlation length κ, shown in Fig. 7(c). Instead of decreasing to the resolution limit at T_m, it remains much larger than the instrumental half-width, 0.016 $Å^{-1}$, all the way to the lowest temperatures. The value of κ is 0.0566 $Å^{-1}$ at 0.43 K, corresponding to an in-plane spin correlation length $\xi(=1/\kappa)$ of only 18 Å.

IV. DATA ANALYSIS

A. General theory for the low-temperature structure

Our analysis is motivated by two observations. First, the atomic structure of $MnCl_2$ in the GIC galleries is virtually identical to that of unintercalated $MnCl_2$. We expect, therefore, that the magnetic parameters associated with in-plane interactions should be unchanged upon intercalation. A striking similarity between the magnetic diffraction patterns of intercalated and pristine $MnCl_2$ suggests that our expectation is well founded. Two magnetic phases are observed for pristine $MnCl_2$.[2] When projected onto the $(hk0)$ plane, all the Bragg peaks in the high-temperature 2×5 rectangular phase coalesce onto a pattern much like that shown in Fig. 2. The main difference is that $\mathbf{k}_1$ is commensurate at Mn (1/10, 1/10, 0) for pristine $MnCl_2$, while for the GIC it is longer and incommensurate, Mn(0.153, 0.153, 0). (The existence of six reflections about each structural Bragg point comes about from the three 120° twins of the 2×5 magnetic cell.) In the low-temperature phase, the projected diffraction pattern is similar, except that each of the six spots in the diffraction halo is split into two, rotated $\pm 10.9°$ from the original spot.

The second observation is that the spin structures of neither $MnCl_2$ nor $MnCl_2$-GIC can be explained by the usual Hamiltonian,[10] and Eq. (1) must therefore be modified. Be-

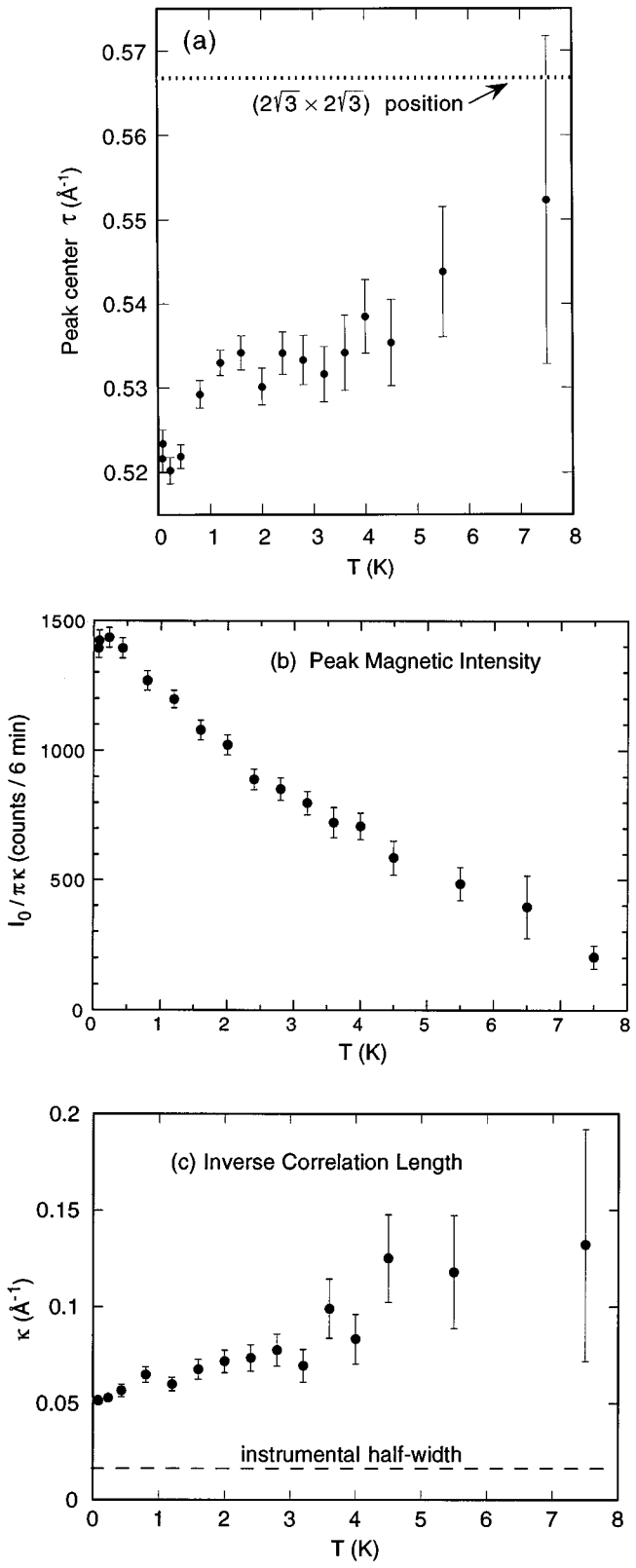

FIG. 7. Temperature dependence of (a) peak position τ for the lowest order magnetic reflection, (b) peak intensity $I_0/\pi\kappa$, and (c) inverse correlation length κ. The instrumental resolution limit for κ is 0.016 Å^{-1}.

cause the materials are insulating we expect only superexchange and dipolar interactions to be significant. Because of the structural and magnetic similarity of the pristine compound to the GIC, we expect that the same Hamiltonian should suffice for both, with small modifications of interaction strengths reflecting their different structures along the c axis.

The addition of weak higher-neighbor exchange terms may have a profound difference on the low-temperature spin structure. For example, Sakakibara[21] has shown that the 120° spin structure with $J_0<0$ is unstable against an infinitesimal interplanar exchange interaction J', and two kinds of incommensurate spin structures appear according to the sign of J_1. Dipolar interactions, as well, can lead to incommensurate structures, as pointed out by Shiba and Suzuki.[22]

We generalize the spin Hamiltonian to consist of the sum of an exchange interaction,

$$H_{\rm ex}=-2\sum_{\langle i,j\rangle} J(\mathbf{R}_{ij})\mathbf{S}_i\cdot\mathbf{S}_j, \tag{4}$$

and a dipole-dipole interaction

$$H_d=(g\mu_B)^2\sum_{\langle i,j\rangle}\frac{1}{R_{ij}^3}\left[\mathbf{S}_i\cdot\mathbf{S}_j-3\frac{(\mathbf{R}_{ij}\cdot\mathbf{S}_i)\cdot(\mathbf{R}_{ij}\cdot\mathbf{S}_j)}{R_{ij}^2}\right]. \tag{5}$$

$\mathbf{S}_i$ is considered a classical XY spin vector at site $\mathbf{R}_i$, $\mathbf{R}_{ij}=\mathbf{R}_i-\mathbf{R}_j$, and $J(\mathbf{R}_{ij})$ is the exchange interaction between the spins $\mathbf{S}_i$ and $\mathbf{S}_j$. The sums run over all pairs of spins.

Alternatively, the total Hamiltonian can be written as a Fourier sum[22]

$$H=-\sum_{\mathbf{q}} J(\mathbf{q})\mathbf{S}_{\mathbf{q}}\cdot\mathbf{S}_{-\mathbf{q}}+\sum_{\mathbf{q}}\sum_{\alpha\beta} S_{\mathbf{q}}^{\alpha}D^{\alpha\beta}(\mathbf{q})S_{-\mathbf{q}}^{\beta}, \tag{6}$$

with

$$\mathbf{S}_i=\frac{1}{\sqrt{N}}\sum_{\mathbf{q}}\mathbf{S}_{\mathbf{q}}\exp(i\mathbf{q}\cdot\mathbf{R}_i),\quad \mathbf{S}_{\mathbf{q}}=\frac{1}{\sqrt{N}}\sum_{i}\mathbf{S}_i\exp(-i\mathbf{q}\cdot\mathbf{R}_i), \tag{7}$$

$$J(\mathbf{q})=\sum_{j(\neq i)} J(\mathbf{R}_{ij})\exp(i\mathbf{q}\cdot\mathbf{R}_{ij}), \tag{8}$$

and

$$D^{\alpha\beta}(\mathbf{q})=\frac{1}{2}(g\mu_B)^2\sum_{j(\neq i)} R_{ij}^{-3}\left(\delta^{\alpha\beta}-3\frac{R_{ij}^{\alpha}R_{ij}^{\beta}}{R_{ij}^2}\right)\exp(i\mathbf{q}\cdot\mathbf{R}_{ij}). \tag{9}$$

N is the number of spins, and α and β run over Cartesian coordinates x,y.

The exchange interactions are assumed to extend to third neighbors in the plane and first neighbors across planes, as illustrated in Fig. 1. Thus,

$$J(\mathbf{q})=J_0(\mathbf{q})+J_1(\mathbf{q})+J_2(\mathbf{q})+J'(\mathbf{q}), \tag{10}$$

where J' is the interplanar exchange constant, and

$$J_0(\mathbf{q})=2J_0[\cos(2\pi H)+\cos(2\pi K)+\cos(2\pi[H+K])], \tag{11}$$

$$J_1(\mathbf{q})=2J_1[\cos(2\pi[H-K])+\cos(2\pi[H+2K])+\cos(2\pi[2H+K])], \tag{12}$$

$$J_2(\mathbf{q}) = 2J_2[\cos(4\pi H) + \cos(4\pi K) + \cos(4\pi[H+K])]. \tag{13}$$

Here $\mathbf{q} = H\mathbf{a}^* + K\mathbf{b}^* + L\mathbf{c}^*$. For simplicity, we assume that the nearest-neighbor Mn^{2+} ions in adjacent layers are in the same positions as for the pristine compound, i.e., at $\pm[(2\mathbf{a}+\mathbf{b})/3+\mathbf{c}]$, $\pm[(\mathbf{a}+2\mathbf{b})/3+\mathbf{c}]$, and $\pm[(\mathbf{a}-\mathbf{b})+\mathbf{c}]$. Then the interplanar exchange interaction is

$$J'(\mathbf{q}) = 2J'\left[\cos\left\{\frac{2\pi}{3}(2H+K+L)\right\} + \cos\left\{\frac{2\pi}{3}(-H+K+L)\right\} + \cos\left\{\frac{2\pi}{3}(-H-2K+L)\right\}\right]. \tag{14}$$

Out-of-plane exchange interactions can be ignored for $MnCl_2$-GIC, since there is no evidence of interlayer coupling.

B. Helical spin configuration

The incommensurate magnetic wave vector suggests a helical configuration with spins confined to the easy plane:

$$S_j = S[\cos(\tau\cdot\mathbf{R}_j + \phi)\hat{\mathbf{x}} + \sin(\tau\cdot\mathbf{R}_j + \phi)\hat{\mathbf{y}}], \tag{15}$$

where $\hat{\mathbf{x}}$ and $\hat{\mathbf{y}}$ are the unit vectors in the xy-plane and ϕ is an arbitrary phase factor. For such a configuration, $\mathbf{S_q} = 0$ for $\mathbf{q} \neq \pm\tau$, and the ground-state energy of the system is

$$U_G = -2\tilde{J}(\tau)\mathbf{S}_\tau\cdot\mathbf{S}_{-\tau} = -NS^2\tilde{J}(\tau), \tag{16}$$

where

$$\tilde{J}(\tau) = \sum_{j(\neq i)}\left[J(\mathbf{R}_{ij}) + \gamma_D\left(\frac{a}{R_{ij}}\right)^3\left(\frac{x_{ij}^2 + y_{ij}^2 - 2z_{ij}^2}{R_{ij}^2}\right)\right] \times \exp(i\tau\cdot\mathbf{R}_{ij}). \tag{17}$$

Following Sakakibara,[21] we determine the minimum-energy configuration by maximizing $\tilde{J}(\tau)$ with respect to τ.

We expect dipole-dipole interactions to be much weaker than the exchange interaction. The nearest-neighbor shell contributes at most $\gamma_D = (g\mu_B)^2/4a^3 = 12$ mK per spin to the dipole energy. In comparison, the mean-field approximation predicts a Curie-Weiss temperature of

$$\Theta = \tfrac{2}{3}S(S+1)6\langle J\rangle. \tag{18}$$

With $\Theta = -5.94$ K for $MnCl_2$-GIC, $\langle J\rangle = -170$ mK, which is much larger in magnitude than the leading dipole term. The dipole contribution will thus be a small (but non-negligible) perturbation to the configuration dictated by exchange forces.

Bearing this in mind, we have numerically evaluated the ground-state energy given by Eqs. (16) and (17), initially ignoring terms including J' and γ_D. For each of two parameters—$J_1/|J_0|$ and $J_2/|J_0|$—we have determined the position of the wave vector τ that minimizes the energy U_G. The two resulting phase diagrams—one each for $J_0 > 0$ (ferromagnetic) and $J_0 < 0$ (antiferromagnetic)—are shown in Figs. 8(a) and 8(b). Different phases are described by their in-plane wave vector (H,K), referenced to the $MnCl_2$ sublattice. A few values of η are shown in the

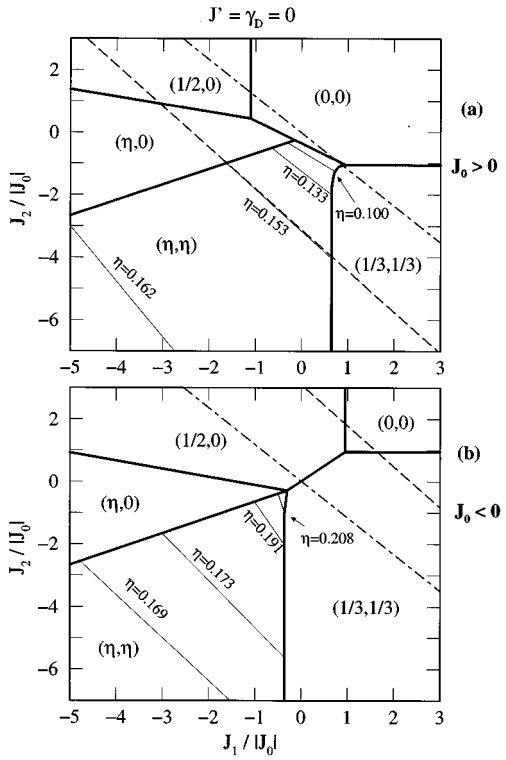

FIG. 8. $T = 0$ phase diagrams for $J' = 0$ and no dipole-dipole coupling: (a) ferromagnetic and (b) antiferromagnetic near-neighbor coupling. Phases are denoted by their modulation wave vector (H,K), and phase boundaries are shown as bold solid lines. $MnCl_2$-GIC and $MnCl_2$ lie in the (η,η) region, in which several lines of constant η are shown. The dashed line is the condition of minimum energy for $\tau = (0.153, 0.153)$ after Eq. (19); any such solutions above and to the right of the dash-dotted line [Eq. (20)] are disallowed, as in (b).

(η,η) region, where $MnCl_2$ and $MnCl_2$-GIC lie (at $\eta = 0.10$ and 0.153, respectively).

By Eq. (16), $\partial U_G/\partial H$ and $\partial U_G/\partial K$ both vanish at $H = K = 0.153$ for $MnCl_2$-GIC. In the absence of dipolar terms, this requires

$$\zeta_2 = -1.315\zeta_1 - 3.107, \tag{19}$$

where $\zeta_1 = J_1/J_0$ and $\zeta_2 = J_2/J_0$. Equation (19) is drawn as dashed lines in Figs. 8(a) and 8(b). Furthermore, the second derivatives of U_G with respect to H and K must be positive at $H = K = 0.153$, leading to an inequality

$$J_0(\zeta_2 + 1.171\zeta_1 + 0.017) < 0. \tag{20}$$

The inequality is satisfied on the lower left side of the dot-dashed lines in Figs. 8(a) and 8(b). Comparison of Eqs. (19) and (20) shows that solutions describing $MnCl_2$-GIC are possible only for $J_0 > 0$.

The effect of dipole coupling on these phase diagrams is shown in Figs. 9(a) and 9(b) for the (rather extreme) case of $\gamma_D = |J_0|$. The first figure ($J_0 > 0$) is modified mostly by increasing the range of stability of the (η,η) phase and by pushing the lines of constant η to smaller J_1 and smaller J_2. The second ($J_0 < 0$) is changed more dramatically, but the main effect is also to push lines of constant η to smaller

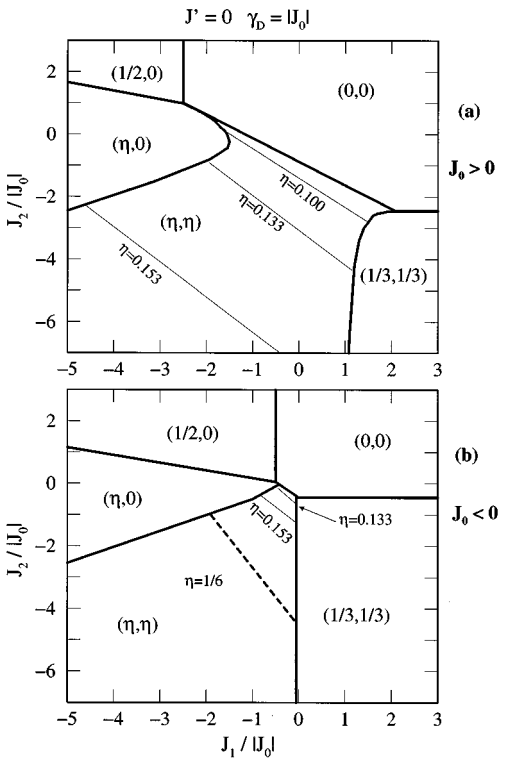

FIG. 9. Same as Fig. 8, but with a dipole-dipole coupling of strength $\gamma_D = |J_0|$.

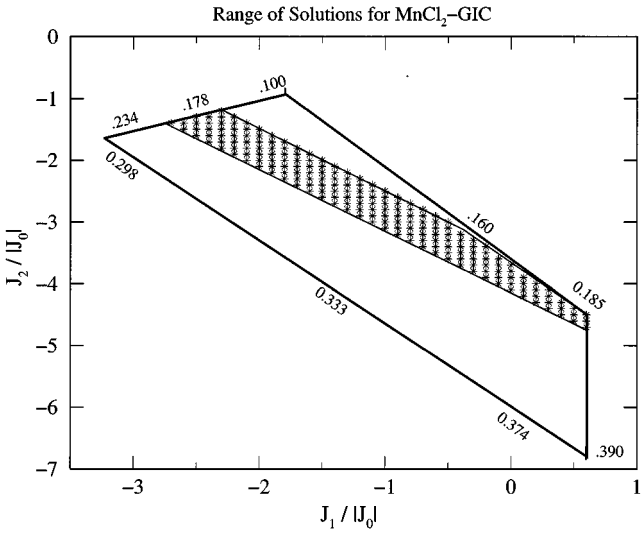

FIG. 10. Smaller region of the phase diagram projected onto the J_1-J_2 plane for J_0 ferromagnetic. The large quadrilateral denotes the range of solutions consistent with the high-temperature susceptibility data and the observed modulation wave vector. The numbers refer to representative values of γ_D/J_0. The smaller shaded region denotes the subset of these solutions for which the energy minimum would occur at the $MnCl_2$ modulation wave vector with the addition of a suitable J'.

J_1 and smaller J_2. Both diagrams show regions of stability for the observed GIC structure ($\eta = 0.153$), but only for $J_2 < 0$. We have verified this condition for all values of γ_D. The results demonstrate that at least three in-plane interaction terms are required to explain our data.

We expect the true phase diagram to be intermediate between Figs. 8(a) and 9(a). Combining the numerical values of the dipole strength $\gamma_D = 12$ mK and the Curie-Weiss temperature $\Theta = -5.94$ K [Eq. (18)] yields the empirical constraint,

$$\frac{\Delta E}{J_0} \equiv \zeta_1 + \zeta_2 + 1 + 14.1\left(\frac{\gamma_D}{J_0}\right) = 0. \tag{21}$$

Because of uncertainties in Θ (roughly ± 0.5 K), we consider all solutions for which ΔE is close (within $0.3|J_0|$) to zero. With this constraint, solutions for $J_0 > 0$ are limited to $\gamma_D < 0.4|J_0|$. As expected from the analysis above, there are no legitimate solutions for $J_0 < 0$: The minimum ΔE there is about $16|J_0|$.

The range of valid solutions is shown in Fig. 10, delimited by the large quadrilateral. Values of $\gamma_D/|J_0|$ are shown at some positions along the perimeter. For all legitimate solutions, J_2 is less than zero and at least as strong as the near-neighbor coupling J_0.

If the in-plane exchange terms are unaffected by intercalation,[23] we may use the pristine $MnCl_2$ data to derive a further constraint. For each of the values of J_0, J_1, J_2 and γ_D consistent with the observed GIC result, we calculate via Eqs. (16) and (17) the minimum energy configuration for the $MnCl_2$ lattice (i.e., for closer layer spacing) as a function of interplanar coupling strength J'. The shaded region in Fig. 10 is the subset of those parameters for which the energy minimum can be made to occur at $\eta = 1/10$, the wave vector for the pristine compound, by any choice of J'. In this region $\gamma_D = (0.19 \pm 0.03)|J_0|$, $J' = \pm(16 \pm 3)|J_0|$, and J_1 and J_2 covary such that $J_1 + J_2 = (-3.9 \pm 0.3)|J_0|$. Sets of parameters at various spots within both the large and small solution ranges of Fig. 10 are put on an absolute scale and displayed in Table I.

V. DISCUSSION

A. Low-temperature structure

The most important aspect of our results is the surprising strength of distant neighbors in the exchange Hamiltonian. Although second-neighbor exchange interactions are sometimes larger than those for first neighbors, as in the case of MnO and NiO,[24] this is rare. We are unaware of any other insulating magnetic system for which three in-plane ex-

TABLE I. Representative solutions: $MnCl_2$-GIC low-temperature magnetic structure. The first four rows correspond to the four corners of the large quadrilateral in Fig. 10. The shaded region of Fig. 10, corresponding to solutions valid for both the pristine and intercalation compounds, roughly interpolates the last two rows here.

J_1/J_0	J_2/J_0	γ_D/J_0	J_0 (mK)	J_1 (mK)	J_2 (mK)	J'-pris (K)
−3.1	−1.8	0.298	40	−120	−70	
−1.9	−1.0	0.114	100	−150	−80	
0.6	−6.8	0.390	30	20	−210	
0.6	−4.5	0.185	60	40	−290	±1.0
−2.5	−1.3	0.178	70	−170	−90	±1.0

change couplings are required, let alone for which the third neighbor exchange is likely the strongest. Both J_1 and J_2 are mediated through two intervening anions in a Mn^{2+}-Cl^--Cl^--Mn^{2+} bridge. Since the overlap of wave functions of the neighboring Cl^- ions is small, one would expect that both these paths would lead to negligibly small couplings. Yet at least one, and perhaps both, of them is stronger than the nearest-neighbor coupling.

In absolute magnitude, the second- and third-shell couplings are not unusually large, being on the same order (a few K or tenths of K) as next-nearest-neighbor interactions in other transition metal dichlorides.[6,25] What distinguishes $MnCl_2$ from the other compounds is an unusually small near-neighbor coupling, which gives more importance to more distant neighbors. For $MnCl_2$-GIC, J_0 is less than 100 mK, in contrast with 14 K for $CoCl_2$ [Ref. 25] or 22 K for $NiCl_2$.[6]

What causes J_0 to be both small and ferromagnetic? The electron configuration of Mn^{2+} is given by $d\varepsilon^3 d\gamma^2$, where the threefold $d\varepsilon(t_{2g})$ levels lie lower than the twofold $d\gamma(e_g)$ level. The $d\gamma$ orbitals have six lobes pointing toward near-neighbor Cl^- anions; partial covalency is manifested by bonds involving these. The $d\varepsilon$ orbitals have twelve lobes, each pointing 45° from the Mn-Cl bonds. Both orbitals are sketched in the bottom panel of Fig. 11(b).

The near-neighbor superexchange path proceeds through two Mn^{2+}-Cl^- bonds which, because of the octahedral coordination, are nearly perpendicular to each other [see Fig. 11(a)]. Such ''90° superexchange'' interactions have been discussed by Goodenough[26] and Kanamori.[27] Antiferromagnetic correlations are expected by most mechanisms. The quasidirect exchange, Mn^{2+}-Mn^{2+} (in Goodenough's notation) favors antiferromagnetism, since sharing of electrons between Mn^{2+} ions is possible only if the electron spins are antiparallel. Similarly, partial bonds can be formed between either the $d\varepsilon$ and $p\pi$ orbitals, the $d\gamma$ and $p\sigma$ orbitals, or the $d\gamma$ and s orbitals of Mn^{2+} and Cl^-, respectively. In these cases, partial transfer of electrons from the Cl^- to each Mn^{2+} can be accomplished only if the Mn^{2+} spins are antialigned, leading again to antiferromagnetic coupling. The only mechanism leading to ferromagnetic exchange[26,27] is the simultaneous transfer of electrons from a Cl^- anion from two different p orbitals, so that each forms a partial $d\varepsilon$-$p\sigma$ bond with nearest-neighbor Mn^{2+} ions. Hund's first rule favors the spins remaining on the Cl^- to be aligned, giving a net ferromagnetic interaction between the Mn^{2+} spins.

This effect is expected to be much smaller than the antiferromagnetic correlations until the $d\varepsilon$ orbitals become more than half filled,[26] as for $CoCl_2$ and $NiCl_2$, for which ferromagnetic nearest-neighbor interactions are well established.[6,25] In fact, it is widely believed on the basis of high-temperature susceptibility that the antiferromagnetic term wins out for the case of $MnCl_2$. Our results demonstrate that this is not true: The negative Curie-Weiss temperature is instead a consequence of the more distant-neighbor antiferromagnetic terms. The low value of J_0 we report indicates that the terms favoring antiferromagnetic and ferromagnetic superexchange are very nearly balanced.

In most of the range of solutions (Fig. 10), J_2 is stronger than J_1. To understand why this might be true, we first recognize that both interactions must be mediated through a

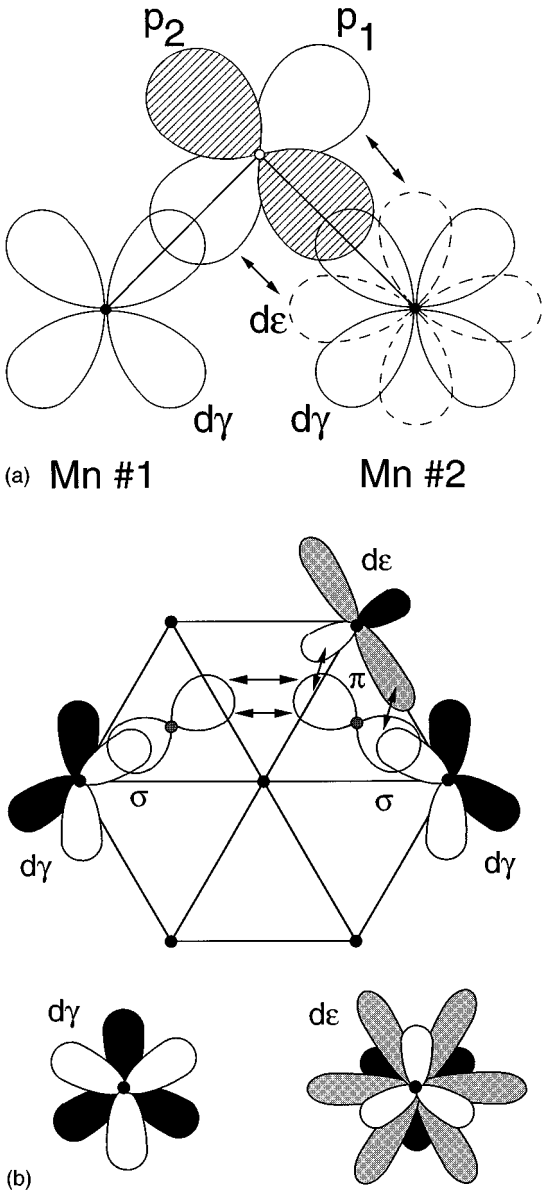

FIG. 11. (a) Schematic of the near-neighbor interaction in the Mn^{2+}-Cl^--Mn^{2+} plane. Two competing effects give a small J_0: Delocalization superexchange of the p_1 electrons in a partial σ-bond with Mn #1 ($d\gamma$-$p\sigma$) and a π bond with Mn #2 ($d\varepsilon$-$p\pi$, shown by the arrows) leads to antiferromagnetic correlations. Simultaneous partial σ-bond formation of the Cl^- with Mn #1 (p_1-$d\gamma$) and Mn #2 (p_2-$d\gamma$) gives ferromagnetic correlations since the remaining (untransferred) p electrons prefer to be aligned because of Hund's rule. (b) Projection onto the intercalate plane of the d and p orbitals of Mn^{2+} and Cl^- involved in the double-anion superexchange. Black orbital lobes extend below the plane, gray ones are in the plane, and white ones rise above the plane. The two Cl^- ions shown are above the plane. (All the lobes of the $d\gamma$ and $d\varepsilon$ orbitals are shown in the bottom panel.) J_1 requires one $d\gamma$-$p\sigma$ and one $d\varepsilon$-$p\pi$ bond, while J_2 involves two $d\gamma$-$p\sigma$ bonds and is therefore stronger.

double anion bridge involving the same anions: Mn^{2+}-Cl^--Cl^--Mn^{2+}. The reason that J_2 is likely stronger than J_1 is that the longer path involves no π bonds. As shown by a projection onto the a-b plane in Fig. 11(b), two $p\sigma$-d bonds are involved in the bridge for J_2, whereas one of

the bonds must be a $p\pi$ bond for the bridge to J_1. As mentioned above, the absolute size of J_2 is not particularly large; it becomes dominant, though, because of the fortuitous near cancellation of ferro- and antiferromagnetic near-neighbor couplings.[28]

B. Other models

The analysis above has assumed a helimagnetic structure and has attempted to explain the magnetism with the fewest interactions, regardless of their relative strengths. We have also considered two modifications, one involving more distant neighbors and the second involving nonhelimagnetic structures.

In the first, we applied an *ad hoc* constraint that the exchange coupling strengths must decrease with distance, and searched for the simplest model that would explain the $MnCl_2$-GIC data. A successful model was found, details of which appear elsewhere.[17] Four shells of neighbors were needed, with J_0 ferromagnetic and the other three interactions antiferromagnetic. We find this solution less attractive, however, than the one presented above: fourth-neighbor interactions must involve three intermediate Cl^- ions in the superexchange bridge, and the coupling should decrease much faster with distance than this model predicts.[26]

Our second modification was nonhelimagnetic configurations. We considered two such structures: a stripe-domain Ising phase and a phase with spins confined to any of the six equivalent hexagonal directions. The first of these models is motivated by the structure proposed for $MnCl_2$ by Wilkinson *et al.*[2] The second model is suggested by reports of a sixfold in-plane anisotropy field in $CoCl_2$-GIC.[29] In both cases, higher-order Bragg reflections are expected (all odd orders for the stripe-domain model and for the hexagonally locked-in structure all of order $6n\pm1$ for integers n). These are not seen in either the pristine data[2] or in the GIC data; however, the higher-order reflections might be so weak that they are not observed.

In order to treat these models, our analysis is modified by first writing the spins as an appropriate Fourier sum:

$$\mathbf{S}_j = S\sum_n (F_n\hat{\mathbf{x}} + G_n\hat{\mathbf{y}})\exp(in\tau\cdot\mathbf{R}_j). \tag{22}$$

The exchange energy is then

$$U_{\rm ex} = -S^2\sum_n (F_nF_{-n} + G_nG_{-n})J(n\tau), \tag{23}$$

which now includes higher order terms of $J(\tau)$. The dipole-dipole energy derives in a similar way. Phase diagrams based on these models are qualitatively similar to those in Figs. 8 and 9. Without field-dependent measurements on a single crystal, such as those performed for the pristine compound,[3] we cannot conclusively say that $MnCl_2$-GIC is a helimagnet. However, even for these more complicated models, the two main results of our analysis persist—namely, that J_0 is weak and ferromagnetic and that a third-neighbor in-plane exchange term is necessary to explain the magnetic structure. More precise values of the exchange parameters will require further study of the spin-wave dispersion by inelastic neutron scattering.

C. Critical behavior

One of our motivations for this study was to evaluate the suitability of $MnCl_2$-GIC as a magnetic prototype of the classical 2D AFT. The complexity of the interactions indicates that it is not well suited to test these simpler models experimentally. Two features of the data, though, merit comment. First, the phase transition seen in the ac susceptibility measurements[12] is not apparent in the neutron data. Instead, we observe a monotonic increase of the correlation length to the lowest temperatures, rather than a divergence associated with the 1.1 K susceptibility maximum. These features are consistent with spin-glass behavior. Other spin glasses, for example $Au_{1-x}Fe_x$ and $Au_{1-x}Cr_x$ (Ref. 30), show similar temperature dependence of the correlation length and peak intensity. It is worth noting that the results of previously reported bulk magnetic measurements on $MnCl_2$-GIC (Ref. 13) are also consistent with spin-glass behavior at T_m: a cusplike behavior in the ac susceptibility; the absence of a heat capacity anomaly; and the onset of irreversibility in the magnetization.

The second interesting feature is the behavior shown in Fig. 7(a), in which the modulation wave vector changes continuously with temperature. As T is raised, the system apparently tries to adopt a local configuration commensurate with the lattice by decreasing the pitch of the helimagnet. Similar coiling behavior has been observed in computer simulations of other 2D triangular spin systems.[31] It would be of interest to test whether simulations using the exchange couplings determined here could reproduce the behavior we have reported and, if so, could shed some light on the critical behavior of $MnCl_2$-GIC.

ACKNOWLEDGMENT

We thank H. Suematsu for providing us with high quality single-crystal kish graphite. The work at SUNY Binghamton was supported by NSF Grant No. DMR 9201656.

*Present address: Laboratory of Cardiac Energetics, National Heart, Lung, and Blood Institute, National Institutes of Health, Bethesda, MD 20892.

[1] C. Starr, F. Bitter, and A. R. Kaufmann, Phys. Rev. **58**, 977 (1940); R. B. Murray and L. D. Roberts, *ibid.* **100**, 1067 (1955); R. B. Murray, *ibid.* **100**, 1071 (1955); R. B. Murray, *ibid.* **128**, 1570 (1962); W. F. Giauque, G. E. Brodale, R. A. Fisher, and E. W. Hornung, J. Chem. Phys. **42**, 1 (1965); M. Regis and Y. Farge, J. Phys. **37**, 627 (1976); A. F. Lorenko, P. E. Parkhomchuk, S. M. Ryabchenko, and P. A. Trotsenko, Sov. Phys. JETP **62**, 714 (1985).

[2] M. K. Wilkinson, J. W. Cable, E. O. Wollan, W. C. Koehler, Oak Ridge National Lab. Report No. ORNL-**2430**, 65 (1957).

[3] M. K. Wilkinson, E. O. Wollan, J. W. Cable, and W. C. Koehler, Oak Ridge National Lab. Report No. ORNL-**2501**, 37 (1958).

[4] M. K. Wilkinson, J. W. Cable, E. O. Wollan, and W. C. Koehler, Phys. Rev. **113**, 497 (1959).

[5] R. C. Chisholm and J. W. Stout, J. Chem. Phys. **36**, 972 (1962).

[6] P. A. Lindgård, R. J. Birgeneau, J. Als-Nielsen, and H. J. Guggenheim, J. Phys. C **8**, 1059 (1975).
[7] M. Suzuki, *Extended Abstracts of the Symposium on Graphite Intercalation Compounds: Science and Applications*, edited by M. Endo, M. S. Dresselhaus, and G. Dresselhaus (Materials Research Society, Pittsburgh, 1988), p. 65.
[8] S. Miyashita and H. Shiba, J. Phys. Soc. Jpn. **53**, 1145 (1984); D. H. Lee, J. D. Joannopoulos, J. W. Negele, and D. P. Landau, Phys. Rev. Lett. **52**, 433 (1984).
[9] J. M. Kosterlitz and D. J. Thouless, J. Phys. C **6**, 1181 (1973); J. M. Kosterlitz, *ibid.* **7**, 1046 (1974).
[10] D. G. Wiesler, M. Suzuki, P. C. Chow, and H. Zabel, Phys. Rev. B **34**, 7951 (1986).
[11] O. Gonzalez, S. Flandrois, A. Maaroufi, and J. Amiell, Solid State Commun. **51**, 499 (1984).
[12] Y. Kimishima, A. Furukawa, M. Suzuki, and H. Nagano, J. Phys. C **19**, L43 (1986).
[13] M. Matsuura, Y. Karaki, T. Yonezawa, and M. Suzuki, Jpn. J. Appl. Phys. **26**, Suppl. 26-3, 773 (1987).
[14] K. Koga and M. Suzuki, J. Phys. Soc. Jpn. **53**, 786 (1984); M. Suzuki, S. M. Sampere, and K. Koga, Phys. Rev. B **39**, 6979 (1989).
[15] M. Suzuki, D. G. Wiesler, P. C. Chow, and H. Zabel, J. Magn. Magn. Mater. **54-57**, 1275 (1986).
[16] D. G. Wiesler, M. Suzuki, I. S. Suzuki, and N. Rosov, Phys. Rev. Lett. **75**, 942 (1995).
[17] M. Suzuki, I. S. Suzuki, D. G. Wiesler, and N. Rosov, J. Phys. Chem. Solid **57**, 729 (1996).
[18] C. Escribe, J. Bouillot, and K. R. A. Ziebeck, J. Phys. C **13**, 4053 (1980).
[19] J. S. Speck, J. T. Nicholls, B. J. Wuensch, J. M. Delgados, and M. S. Dresselhaus, Philos. Mag. B **64**, 181 (1991).
[20] S. Hendricks and E. Teller, J. Chem. Phys. **10**, 147 (1942).
[21] T. Sakakibara, J. Phys. Soc. Jpn. **53**, 3607 (1984).
[22] H. Shiba and N. Suzuki, J. Phys. Soc. Jpn. **51**, 3488 (1982).
[23] Despite its intuitive appeal, this assumption may not hold precisely, especially since the superexchange coupling depends on the electronic environment of the Cl^- ions, which is altered slightly by intercalation. Spin-wave dispersion measurements in $CoCl_2$-GIC, for example, have shown that J_0 is significantly reduced in the intercalation compound from what it is in the pristine compound. See H. Zabel and S. M. Shapiro, Phys. Rev. B **36**, 7292 (1987) and Ref. 25. The larger region in Fig. 10 is therefore a more conservative, and perhaps ''better'' estimate of the range of solutions.
[24] M. T. Hutchings and E. J. Samuelsen, Solid State Commun. **9**, 1011 (1971); M. E. Lines and E. D. Jones, Phys. Rev. **139**, A1313 (1965).
[25] M. T. Hutchings, J. Phys. C **6**, 3143 (1973).
[26] J. B. Goodenough, *Magnetism and the Chemical Bond* (Interscience Publishers, New York, 1963).
[27] J. Kanamori, J. Phys. Chem. Solid **10**, 87 (1959).
[28] Since strong third-neighbor interactions seem to be the consequence of the lattice geometry, it is possible that third-neighbor interactions are comparable to second-neighbor ones in other transitions metal dichlorides, as well as $MnCl_2$. This situation would have less of an effect on the structure, though, since J_0 is so much larger there.
[29] M. Elahy and G. Dresselhaus, Phys. Rev. B **30**, 7225 (1984).
[30] A. P. Murani, Phys. Rev. Lett. **37**, 450 (1976); Y. Nakai, M. Sakuma, and N. Kunitomi, J. Phys. Soc. Jpn **56**, 301 (1987).
[31] W. M. Saslow, M. Gabay, and W.-M. Zhang, Phys. Rev. Lett. **68**, 3627 (1992).